Information Sciences 259 (2014) 128–141

Contents lists available at ScienceDirect

Information Sciences

journal homepage: www.elsevier.com/locate/ins

Joint image denoising using adaptive principal component analysis and self-similarity

Yongqin Zhang, Jiaying Liu, Mading Li, Zongming Guo *

Institute of Computer Science and Technology, Peking University, Beijing 100871, China

ARTICLE INFO

Article history:
Received 11 April 2013
Received in revised form 1 July 2013
Accepted 3 August 2013
Available online 11 August 2013

Keywords:
Image denoising
Dimensionality reduction
Principal component analysis
Singular value decomposition
Parallel analysis

ABSTRACT

The non-local means (NLM) has attracted enormous interest in image denoising problem in recent years. In this paper, we propose an efficient joint denoising algorithm based on adaptive principal component analysis (PCA) and self-similarity that improves the predictability of pixel intensities in reconstructed images. The proposed algorithm consists of two successive steps without iteration: the low-rank approximation based on parallel analysis, and the collaborative filtering. First, for a pixel and its nearest neighbors, the training samples in a local search window are selected to form the similar patch group by the block matching method. Next, it is factorized by singular value decomposition (SVD), whose left and right orthogonal basis denote local and non-local image features, respectively. The adaptive PCA automatically chooses the local signal subspace dimensionality of the noisy similar patch group in the SVD domain by the refined parallel analysis with Monte Carlo simulation. Thus, image features can be well preserved after dimensionality reduction, and simultaneously the noise is almost eliminated. Then, after the inverse SVD transform, the denoised image is reconstructed from the aggregate filtered patches by the weighted average method. Finally, the collaborative Wiener filtering is used to further remove the noise. The experimental results validate its generality and effectiveness in a wide range of the noisy images. The proposed algorithm not only produces very promising denoising results that outperforms the state-of-the-art methods in most cases, but also adapts to a variety of noise levels.
© 2013 Elsevier Inc. All rights reserved.

1. Introduction

Image denoising is still a challenging problem in the fields of image processing and computer vision. It refers to the recovery of a digital image that has been contaminated by some types of noise, e.g., Gaussian noise, or Rician noise, while preserving image features such as the edges and the textures. The problem of image denoising [34,29] was first studied in 1970s. After the development of wavelet transform in late 1980s, many denoising methods based on wavelet transform and its variants have appeared in the literatures [13,39,6,17,40,35]. However, they often blur the sharp edges and smooth out the fine structures.

Since the non-local means (NLM) algorithm [5] was published by Buades et al., many more powerful denoising techniques have been proposed in the past several years [1,14,30,15,9,42,52,53,12,27,56,2,55,21,31]. After a brief review, there are two basic categories for image denoising approaches. One of them is the spatial filters, which can be further classified into linear filters and non-linear filters. Some of the recent popular linear spatial filters are bilateral filtering [38], Wiener filtering [18], NLM [5] and Total Least Squares (TLS) [23]. Furthermore, many variants of the NLM method [5] were also developed to improve its weight calculation, e.g., Stein's unbiased risk estimate (SURE) [43,36], the principle neighborhood dictionary (PND) [42] and the MMSE approach [28]. Similarly, the typical non-linear spatial filters are total variation regularization

* Corresponding author. Tel.: +86 10 82529641; fax: +86 10 82529207.
E-mail address: guozongming@pku.edu.cn (Z. Guo).

0020-0255/$ - see front matter © 2013 Elsevier Inc. All rights reserved.
http://dx.doi.org/10.1016/j.ins.2013.08.002

(TV) [37], Kernel Regression (KR) [41] and the diffusion filter [4]. The other category is transforming domain filtering methods, which can also be further divided into the non-data adaptive transforms including wavelet-based variants [40,35] and data adaptive transforms, such as K-SVD [1], BM3D [9], principal component analysis (PCA) [54,10] and independent component analysis (ICA) [8].

One main direction of these works is to find sparse representations of signals built on the globally or locally adaptive basis. Assuming that each image patch can be sparsely represented, K-SVD algorithm [1] and its variant [51] learn a sparse and redundant basis of image neighborhoods to remove noise. But they ignore the characteristics of the human visual perception that the edges and textures of the image contribute greatly to the subjective assessment of image quality. The KR method with recursive iterations proposed by Takeda et al. [41] has expensive computation, which is difficult to achieve real-time processing. He et al. [22] proposed an image denoising method using the adaptive thresholding scheme by singular value decomposition. However, its denoising performance depends on three free parameters, which are quite tricky and difficult to tune for optimal values. The patch-based PLPCA method [10] adopts the hard thresholding technique directly for the elements of the eigenvectors, whereas it also damages the sharp edges and the fine structures. Furthermore, its thresholding value is based on the known noise deviation. However, in fact, the noise deviation is unknown in most cases. To the best of our knowledge, the best existing state-of-the-art filtering methods are mostly based on the optimal Wiener filter [9] or equivalently Linear-Minimum Mean Squared Error (LMMSE) [54]. Although they have very good performance for reducing additive white Gaussian noise (AWGN) from the noisy image, they have not yet reached the limit of noise removal [7].

These denoising methods mentioned above have the drawback that while removing noise, they may also smooth the edges and the fine structures in the image. To mitigate this drawback, different from the existing denoising methods, we propose an advanced denoising algorithm based on adaptive principal component analysis and self-similarity (APCAS). The proposed algorithm consists of two successive steps without iteration: the low-rank approximation based on parallel analysis, and the collaborative filtering. The image self-similarity is exploited to construct similar patch groups. Parallel analysis is used to choose the signal dimensionality of the coefficients in the SVD domain of the similar patch group. This dimensionality reduction technique can adaptively determine the number of signal components in noisy environments. The low-rank approximation of the true image is employed to perform the empirical Wiener filtering to further reduce the noise. Our main contributions of the proposed algorithm include the joint denoising strategy without iteration, the self-similarity based image patch clustering and parallel analysis based adaptive principal component analysis for the low-rank approximation. Experimental results show that the proposed algorithm achieves highly competitive performance with the best state-of-the-art methods from subjective and objective measures of image quality, and can outperform them in most cases.

The rest of this paper is organized as follows. In Section 2, the proposed APCAS algorithm for image denoising is described. Section 3 shows the simulation and experimental results of the developed algorithm, and the comparison to the state-of-the-art methods. Finally, the discussions and conclusions are drawn in Section 4.

2. Proposed denoising algorithm

2.1. Method preview

In real-world digital-imaging devices, the acquired images are often contaminated by device-specific noise. Due to the existence of random noise in the acquisition process, magnetic resonance (MR) images are generally the most noisy. In the MR literatures [20,32], the noise in MR images is assumed to be Rician distributed with uniform or non-uniform variance across the image. However, Most of denoising methods in the literatures [9,54,10] have been developed assuming a Gaussian noise distribution with a spatially independent variance. In fact, the Gaussian assumption could be valid on MR images when SNR is larger than two [20]. For simplicity, the additive Gaussian noise model is adopted to simulate the noisy MR images for validation and evaluation of the denoising methods. As in the previous literatures [9,54,10], a simple noise model of independent additive type is generally used to describe the noisy image for simulation in the following formula:

$$y(x) = s(x) + \upsilon(x) \tag{1}$$

where x is a two-dimensional spatial coordinate; y is the observed image, s is the ideal noise-free image, and υ represents additive white Gaussian noise (AWGN) with zero mean and standard deviation σ_n.

Besides giving an image an undesirable appearance, the noise can cover and reduce the visibility of certain features within the image, which weakens the clinical diagnostic accuracy. Thus, it is necessary to remove the noise from MR images. Because of its advantage of not increasing the acquisition time and motion artifacts, postprocessing filtering techniques have been traditionally and extensively used in MR image denoising. In brief, the overview of procedures of our proposed method is described as follows (See Fig. 1):

1 Image pacth clustering. For each target patch, its corresponding patch group is formed by finding similar patches in the observed noisy image.
2 Signal dimension estimation. Parallel analysis is used to estimate the signal dimension of each similar patch group.
3 SVD-based low-rank approximation. The denoised image is obtained with the weighted averaging of the aggregate filtered patches that are constructed with the low-rank approximation.

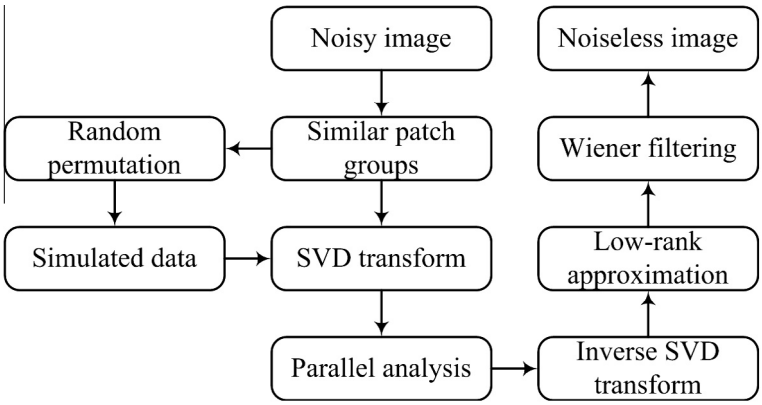

Fig. 1. The workflow of the proposed APCAS algorithm.

Empirical Wiener filtering. With shrinkage coefficients from the denoised result in the first step, the collaborative Wiener filtering further removes the noise.

2.2. Image patch clustering

Since most of the human visual perception and understanding of an image is conveyed by its edge structures and texture patterns. To preserve the edge and the texture, the patch-based image representation is modeled instead of the pixel-based image for noise reduction, where each patch contains a pixel and its nearest neighbors. For an observed noisy image $\mathbf{Y}$ with its coordinate domain $\mathbf{X} \subset \mathbf{R}^{M\times N}$, let $y(x)$ be a pixel at a position x in the image $\mathbf{Y}$. Assuming that P is the number of pixels in the patch, the patch-based image $\mathbf{Y}_x$ denotes a patch of fixed size $\sqrt{P}\times\sqrt{P}$ extracted from $\mathbf{Y}$, where x is the coordinate of the central pixel of the patch. That is, $\mathbf{Y}_x$ is a reshaped vector of size $P\times 1$, which contains the $\sqrt{P}\times\sqrt{P}$ pixels consisting of a central pixel $y(x)$ and its nearest neighbors in the observed image $\mathbf{Y}$.

In order to remove the noise from the input noisy image $\mathbf{Y}$, the data-adaptive SVD transform is used to separate the image signal and the noise. The high degree of self-similarity and redundancy widespreadly exists within any natural image. Through effective analysis of a signal or image, the various sub-dictionaries with atoms should be picked up that are morphologically similar to the features in the signal or image, respectively. For each target pixel $y(x)$ located in the central position of the target patch $\mathbf{Y}_x$, there are totally L possible training patches of the same size $\sqrt{P}\times\sqrt{P}$ in the $\sqrt{L}\times\sqrt{L}$ local search window. However, there may be very different adjacent patches from the given target patch so that taking all the $\sqrt{L}\times\sqrt{L}$ patches as the training samples will cause inaccurate estimation of the target patch vector $\mathbf{Y}_x$. Thus, it is necessary to choose and cluster the training samples that are similar to the target patch for the full use of both local and non-local information before applying the SVD transform. The problem of patch classification has several different solutions, e.g., block matching [9], K-means clustering [3] and affinity propagation (AP) [16]. For simplicity, we employ the block matching method for image patch clustering.

Let $\mathbf{Y}_x = [y_x(1), y_x(2), \ldots, y_x(P)]^T$ denote the central target patch. For typographical convenience, $\mathbf{Y}_l$, $l = 1, 2, \ldots, L-1$ represents the candidate adjacent patches of the same size $\sqrt{P}\times\sqrt{P}$ in the $\sqrt{L}\times\sqrt{L}$ search window Ψ_x. The block matching method is used to construct the patch group based on the similarity measurement between the adjacent patch and the target patch. The relationships between the central pixel, the target patch, the adjacent patch and the local search window can be appreciated in Fig. 2. The similarity metric between the candidate patch and the target patch can be calculated using the Euclidean distance in this formula:

$$e_l = \frac{1}{P}\sum_{p=1}^{P}(y_l(p) - y_x(p))^2 \tag{2}$$

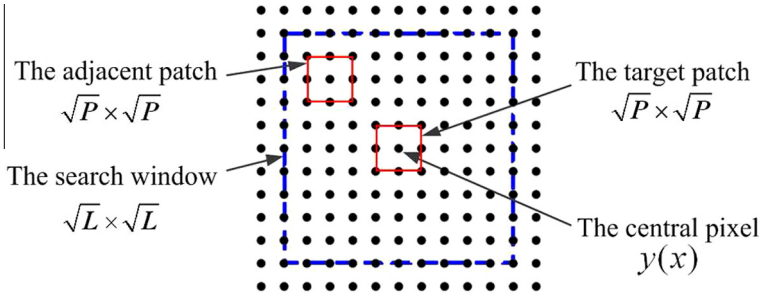

Fig. 2. The relationships between the central pixel, the target patch, the adjacent patch and the local search window.

Then, through the addition of the scalar error 0 between the target patch and itself, we build the error vector $\mathbf{e} = [0, e_1, \ldots, e_{L-1}]^T$. After the error vector $\mathbf{e}$ is sorted in the ascending order, the top most similar patches are chosen to construct the patch group. Assume that we select L_s similar patch vectors to reconstruct the patch group $\mathbf{Z}_x^\upsilon$ for the target patch $\mathbf{Y}_x$, where L_s is a preset number. For each target patch $\mathbf{Y}_x$, its corresponding patch group $\mathbf{Z}_x^\upsilon$ consisting of the training patches can be expressed in this form:

$$\mathbf{Z}_x^\upsilon = [\mathbf{Y}_x, \mathbf{Y}_1, \ldots, \mathbf{Y}_{L_s-1}]^T \tag{3}$$

To separate the image signal and the noise effectively, the number L_s of most similar patches should be large enough. The patch clustering matrix $\mathbf{Z}_x^\upsilon$ or its transposition $(\mathbf{Z}_x^\upsilon)^T$ will be used to avoid the problem of rank deficiency in computing the SVD of the covariance matrix of $\mathbf{Z}_x^\upsilon$. For each noisy measurement $\mathbf{Z}_x^\upsilon$, the next procedure is to estimate its underlying noiseless counterpart dataset $\mathbf{Z}_x = [\mathbf{S}_x, \mathbf{S}_1, \ldots, \mathbf{S}_{L_s-1}]^T$.

2.3. Signal dimension estimation

The PCA operator transfers a set of correlated variables into a new set of uncorrelated variables, whose eigenfunctions form the basis for a signal decomposition. We find that most of the energy of a function defined on the graph is mainly concentrated on the top several principal components. Moreover, the principal components of the original image signal can be captured by analyzing the eigenfunctions generated from noisy data, whereas the eigenvectors of the small singular values are almost all noises. It can also be implemented by eigenvalue decomposition of a data covariance (or correlation) matrix or singular value decomposition (SVD) of a data matrix. Note that the data matrix is usually pre-treated for each attribute by the mean centering method.

The denoising problem of the noisy patch group $\mathbf{Z}_x^\upsilon$ is indeed how to select the optimal number of the principal components in the SVD transform domain. In this paper, we employ dimensionality reduction technique to analyze the eigenvalues of the covariance matrix of the patch group $\mathbf{Z}_x^\upsilon$. By subtracting the sample mean value from each column, we have computed the zero-centered matrix from the patch group $\mathbf{Z}_x^\upsilon$ in this formula:

$$\bar{Z}_x^\upsilon(l,p) = Z_x^\upsilon(l,p) - M_x(l,p) \tag{4}$$

where $M_x(l,p) = [1,\ldots,1]^T \times \frac{1}{L_s}\sum_{l=1}^{L_s} Z_x^\upsilon(l,p); [1,\ldots,1]^T$ is the column vector of size $L_s \times 1$; $l = 1, \ldots, L_s$; and $p = 1, \ldots, P$.

To reduce calculation time in an efficient way on the condition of $L_s \geqslant P$ (or $L_s < P$), the covariance matrix $(\overline{\mathbf{Z}}_x^\upsilon)^T\overline{\mathbf{Z}}_x^\upsilon$ (or $\overline{\mathbf{Z}}_x^\upsilon(\overline{\mathbf{Z}}_x^\upsilon)^T$) instead of the zero-centered patch group $\overline{\mathbf{Z}}_x^\upsilon$ is used to be factorized in this form:

$$(\overline{\mathbf{Z}}_x^\upsilon)^{\mathrm{T}}\overline{\mathbf{Z}}_x^\upsilon = \mathbf{V}\boldsymbol{\Sigma}^2\mathbf{V}^{\mathrm{T}} \tag{5}$$

where the symbol T denotes the transpose operator, and $\mathbf{V}$ is the unitary matrix of eigenvectors derived from $(\overline{\mathbf{Z}}_x^\upsilon)^T\overline{\mathbf{Z}}_x^\upsilon$. Σ is a $P \times P$ diagonal matrix with its singular values $\lambda_1 \geqslant \lambda_2 \geqslant \cdots \geqslant \lambda_r \geqslant 0$ and $r = \mathrm{rank}(\overline{\mathbf{Z}}_x^\upsilon)$.

In fact, the eigenvalues of the covariance matrix of the noise υ are not the same. Therefore, we cannot take a preset fixed threshold to select the signal components. It has been shown in [56] that if the eigenvalues are small enough, the discard of less significant components does not lose much information. From the diagonal singular values, only the first K primary eigenvectors are retained by dimensionality reduction based on parallel analysis. However, the parameter K should be not only large enough to allow fitting the characteristics of the data, but also small enough to filter out the non-relevant noise and redundancy.

There are various dimensionality reduction methods proposed in the literatures for determining the number of components to retain in data analysis. The parallel analysis (PA) method firstly introduced by Horn [24] compares the observed eigenvalues to be analyzed with those of an artificial data set obtained from uncorrelated normal variables. Subsequently, the improvements to the original parallel analysis method have been proposed using Monte-Carlo simulations instead of the normal distribution assumption[26]. It is proved that PA is one of the most successful methods for determining the number of true principal components. In this paper, we adopt the proposed parallel analysis with Monte Carlo simulation to choose the top K largest values.

Let λ_p for $p = 1, \ldots, P$ denote the singular values of the zero-centered patch group $\overline{\mathbf{Z}}_x^\upsilon$ sorted in the descending order. Similarly, let α_p denote the sorted singular values of the artificial data. Therefore, the proposed parallel analysis estimates signal subspace dimensionality of noisy data as follows:

$$K = \max\{p = 1, \ldots, P | \lambda_p \geqslant \alpha_p\} \tag{6}$$

The intuition is that α_p is a threshold value for the singular value λ_p below which the p'th component is judged to have occurred because of chance. Currently, it is recommended to use the singular value that corresponds to a given percentile, such as the 95th of the distribution of singular values derived from the random data set.

In our algorithm, without any assumption of a given random distribution, we generate the artificial data by randomly permuting each element of all the patch vectors located in a search window. Let $y_l(p)$ denote the p'th element of the training patch vector $\mathbf{Y}_l$ (or $\mathbf{Y}_x$) in the patch group $\mathbf{Z}_x^\upsilon$. For each P elements of the patch vector $\mathbf{Y}_l$ (or $\mathbf{Y}_x$), multiple random permutations of the coordinates $p = 1, \ldots, P$ of the noisy data matrix $\mathbf{Z}_x^\upsilon$ are generated by the uniform distribution. Thus, the mean value, maximum, minimum and random distribution of the artificial data is satisfied for each image patch-based vector. Then singular values of the random artificial data are computed by the SVD transform which keeps the marginal distributions intact

while breaking any interdependency between them. For the L_s by P synthetic matrix C_s, after multiple times (e.g. 10) of Monte Carlo simulations, summary statistics (e.g. 95th percentile) can be used to extract the P singular values and order them from the largest to the smallest. Then parallel analysis is applied and the two lines denote singular values of the simulated data C_s and the zero-centered patch group $\overline{\mathbf{Z}}_x^v$, respectively. The intersection of the two lines is the cutoff for determining the number of the signal subspace dimension presented in the noisy image.

While the traditional PCA [44] adopts the thresholding technique to estimate data dimensionality, the proposed adaptive PCA can automatically determine signal subspace dimensions in noisy data by the parallel analysis technique. Our developed refined parallel analysis using Monte Carlo simulation were compared with the traditional PCA [44] for dimensionality reduction in our experiments. Suppose that a 25×25 fragment of *lena* image corrupted by additive zero-mean Gaussian noise with standard deviation 20. In this case, the signal dimensionality of the given noisy patch group $\mathbf{Z}_x^v$ with patch size 5×5 pixels was separately estimated by the proposed adaptive PCA and the traditional PCA [44]. Fig. 3 shows the numbers of its signal subspace dimension estimated by the proposed adaptive PCA technique and the traditional PCA [44] are separately 5 and 19. We can see that the proposed adaptive PCA approach is better than the traditional PCA method for separating the signal and the noise from the noisy image.

2.4. SVD-based low-rank approximation

For each target pixel $y(x)$, the similar candidate patches are selected by the block matching method to form the corresponding patch group $\mathbf{Z}_x^v = [\mathbf{Y}_x, \mathbf{Y}_1, \ldots, \mathbf{Y}_{L_s-1}]^T$. The patch-based correlated patch groups $\mathbf{Z}_x^v$ ($x \in \mathbf{X}$) [see Eq. (3)] can be used for component analysis of the noisy image $\mathbf{Y}$. The zero-centered patch group $\overline{\mathbf{Z}}_x^v$ is factorized by the SVD transform in this formula:

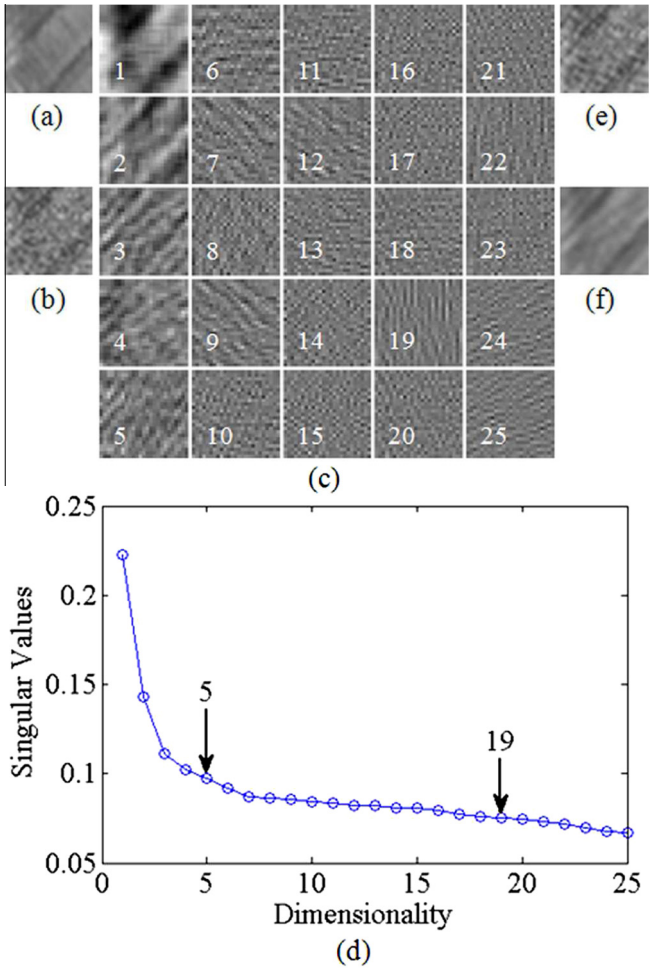

Fig. 3. The eigenimages, the singular values, and the reconstructed images generated from a 25×25 image block with patch size 5×5 pixels of the test *lena* image corrupted by additive zero-mean Gaussian noise with standard deviation 20. (a) the original image block; (b) the noisy image block; (c) the eigenimages; (d) the numbers of its signal subspace dimensionality estimated by the proposed adaptive PCA approach, and the traditional PCA [44] are 5, and 19,respectively; (e) the reconstructed image block ($K = 19$); (f) the reconstructed image block ($K = 5$).

$$\overline{\mathbf{Z}}_x^v = \mathbf{U}\Sigma\mathbf{V}^T \tag{7}$$

where Σ is the diagonal matrix with the singular values $\lambda_1 \geqslant \cdots \geqslant \lambda_r$. $\mathbf{V} = [\mathbf{V}_1, \mathbf{V}_2, \ldots, \mathbf{V}_P]$ and $\mathbf{U} = [\mathbf{U}_1, \mathbf{U}_2, \ldots, \mathbf{U}_{L_S}]$ are the unitary matrices of eigenvectors, which represent the orthogonal dictionaries of non-local bases and local bases, respectively. The zero-centered noisy patch group $\overline{\mathbf{Z}}_x^v$ is decomposed into a sum of components from the largest to the smallest singular values.

In fact, most of the energy of the true image is concentrated on few high-magnitude transform coefficients, whereas the corresponding eigenimages of the small singular values are almost all noises. After automatically determining signal dimension of the noisy zero-centered patch groups $\overline{\mathbf{Z}}_x^v$, the low rank approximation [47,33] is used to estimate the original noiseless image $\mathbf{S}$ by reducing noise in the observed image $\mathbf{Y}$. Through our adaptive signal dimension estimation [see Eq. (6)], the noiseless image can be reconstructed by the SVD-based low rank approach. The straightforward way to restore a noiseless image is to directly apply the inverse SVD transform to the noisy similar patch groups $\mathbf{Z}_x^v$ in a reduced dimensionality representation. That is, the inverse SVD transform is implemented to approximate the true noise-free image with the matrices $\mathbf{\Sigma}_K = \mathrm{diag}\{\lambda_1, \lambda_2, \ldots, \lambda_K\}$, $\mathbf{U}_K = [\mathbf{U}_1, \mathbf{U}_2, \ldots, \mathbf{U}_K]$, and $\mathbf{V}_K = [\mathbf{V}_1, \mathbf{V}_2, \ldots, \mathbf{V}_K]$. For each target pixel, the denoised patch group $\widehat{\mathbf{Z}}_x$ and its weight matrix $\mathbf{W}_x$ are separately estimated as follows:

$$\widehat{\mathbf{Z}}_x = \mathbf{U}_K\mathbf{\Sigma}_K\mathbf{V}_K^T + \mathbf{M}_x \tag{8}$$

$$W_x(l,p) = \begin{cases} 1 - K/P, & K < P \\ 1/P, & K = P \end{cases} \tag{9}$$

where $\mathbf{M}_x$ is the mean value [see Eq. (4)] of the patch group $\mathbf{Z}_x^v$.

After applying such procedures to each pixel $y(x)$, the relevant denoised patch group is estimated with the low rank approach by adaptive PCA technique, and its weight is empirically determined. Since these denoised patches are overlapping, multiple estimates of each pixel in the image are combined to reconstruct the whole image. The weighted averaging procedure is carried out to suppress the noise further. The whole filtered image $\widehat{\mathbf{S}}^t$ is obtained by aggregating all the estimates of each pixel in this formula:

$$\widehat{\mathbf{S}}^t = \frac{1}{\mathbf{W}^t}\sum_{x=1}^{M\times N}\widehat{\mathbf{Z}}_x\mathbf{W}_x \tag{10}$$

where the total weight $\mathbf{W}^t = \sum_{x=1}^{M\times N}\mathbf{W}_x$.

In addition, the proposed efficient algorithm is implemented by reducing the number of the image patch groups. A step of $J_s \in X$ pixels is used for the noisy image in both horizontal and vertical directions. Thus, the number of similar patch groups is approximately MN/J_s^2 rather than MN. Hence most of the noise will be removed by using the adaptive PCA approach and the weighted averaging scheme in Sections 2.2, 2.3, 2.4. However, there is still some unpleasant residual noise in the denoised image, especially for terribly noisy images. As the observed image contains the strong noise, the image patches are seriously corrupted by noise, which leads to image patch clustering errors and the biased estimation of the SVD transform. Consequently, it is necessary to further suppress the noise residual of the denoised output $\widehat{\mathbf{S}}^t$.

2.5. Empirical Wiener filtering

After the first phase of noise removal by the low rank approximation, we can employ the empirical Wiener filtering [9] for the second phase to further improve the denoising performance of the output $\widehat{\mathbf{S}}^t$. Because there is less noise in the output $\widehat{\mathbf{S}}^t$, the close approximation of the true patch distance is calculated with the denoised output $\widehat{\mathbf{S}}^t$ instead of the noisy image $\mathbf{Y}$ [see Eq. (2)]. Thus, the coordinates of the similar patches for each pixel are grouped into the index set:

$$\mathbf{\Omega}_x = \left\{ x \in X : \left\| \widehat{\mathbf{S}}_l^t - \widehat{\mathbf{S}}_x^t \right\|_2^2 / P_x < \tau \right\} \tag{11}$$

where $\widehat{\mathbf{S}}_x^t$ is the $\sqrt{P_x} \times \sqrt{P_x}$ target patch with its central pixel $\hat{s}^t(x)$ in the denoised output $\widehat{\mathbf{S}}^t$; $\widehat{\mathbf{S}}_l^t$ is the $\sqrt{P_x} \times \sqrt{P_x}$ candidate patch in the local search window; $\|\cdot\|_2^2$ is the squared ℓ^2-norm; and τ is a threshold value.

Then the index set $\mathbf{\Omega}_x$ is used to construct two patch groups $\widehat{\mathbf{S}}_{\Omega_x}^t$ and $\mathbf{Y}_{\Omega_x}$ from the denoised output $\widehat{\mathbf{S}}^t$ and the observed noisy image $\mathbf{Y}$, respectively. From the power spectrum coefficients of 3D transform of the denoised patch group $\widehat{\mathbf{S}}_{\Omega_x}^t$, the empirical Wiener shrinkage coefficients for the case of additive white noise are found as:

$$\mathbf{G}_{\Omega_x} = \frac{\left| T_{3D}^{wie}\left(\widehat{\mathbf{S}}_{\Omega_x}^t\right)\right|^2}{\left| T_{3D}^{wie}\left(\widehat{\mathbf{S}}_{\Omega_x}^t\right)\right|^2 + \sigma^2} \tag{12}$$

where σ^2 is the noise variance.

Subsequently, the empirical Wiener filtering of the noisy patch group $\mathbf{Y}_{\Omega_x}$ is executed though multiplying the 3D transform coefficients $T_{3D}^{wie}(\mathbf{Y}_{\Omega_x})$ by the Wiener shrinkage coefficients $\mathbf{G}_{\Omega_x}$. Whereafter, the estimated noiseless patch group is acquired by the inverse 3D transform as follows:

$$\widehat{\mathbf{S}}_{\Omega_x}^{wie} = T_{3D}^{wie^{-1}}\left(\mathbf{G}_{\Omega_x} T_{3D}^{wie}(\mathbf{Y}_{\Omega_x})\right) \tag{13}$$

Note that such an empirical Wiener filter is adaptive because its weight coefficients depend on the spectrum of the output image $\widehat{\mathbf{S}}^t$. However, the patch-wise estimation for each pixel is generally biased, correlated, and have different variances. Moreover, the total sample variance in the corresponding estimates of the patch groups is $\sigma^2\|\mathbf{G}_{\Omega_x}\|_2^2$ on the assumption that the additive noise is signal-independent. To suppress these distortions, the aggregation weights are empirically assigned for the estimates of the patch groups $\widehat{\mathbf{S}}_{\Omega_x}^{wie}$ as follows:

$$\mathbf{W}_{\Omega_\mathbf{x}} = \sigma^{-2}\|\mathbf{G}_{\Omega_x}\|_2^{-2} \tag{14}$$

Therefore, after a weighted average of the patch-wise estimates, the final noiseless image $\widehat{\mathbf{S}}^f$ is obtained as:

$$\widehat{\mathbf{S}}^f = \frac{\sum_{x=1}^{M\times N}\mathbf{W}_{\Omega_x}\widehat{\mathbf{S}}_{\Omega_x}^{wie}}{\sum_{x=1}^{M\times N}\mathbf{W}_{\Omega_x}}, \quad \forall x \in X \tag{15}$$

2.6. Algorithm summary

The following pseudo codes give further clarification of the specific implementation of the proposed algorithm for an input noisy image:

Algorithm 1. Pseudocode of the Proposed Algorithm

Input: $\mathbf{Y}^{M\times N}$,P,L and L_s.
Output: $\widehat{\mathbf{S}}^f$
for each x = 1 to $M \times N$ **do**
/*Convert the pixel-based image to the patch-based image */
$H(x, 1:P) \leftarrow Y\left(m+1:\sqrt{P}, n+1:\sqrt{P}\right)$;
end for
/*The SVD-based low-rank approximation using parallel analysis */
$\widehat{S}^t = \text{zeros}(M\times N, P)$; W^t = zeros ($M \times N$, P);
for each x = 1 to $M \times N$ **do**
$\Psi_x \leftarrow L$; $Y_x = H(x, :)$; $\quad Y_{\Psi_x} = H(\Psi_x, :)$;
$\Psi_x^s = \text{BlockMatching}(Y_x, Y_{\Psi_x}, L_s)$;
$Z_x^v = H(\Psi_x^s, :)$; $M_x = \text{mean}(Z_x^v)$;
$\bar{Z}_x^v = Z_x^v - M_x$; $(\bar{Z}_x^v)^T\bar{Z}_x^v = V\Sigma^2V^T$; $C^TC = V\Lambda^2V^T$;
λ = diag (Σ); α = diag (Λ);
K = max{p = 1, …, P—$\lambda_p \geqslant \alpha_p$};/*Parallel analysis */
$\widehat{Z}_x = U_K\Sigma_KV_K^T + M_x$;
$\widehat{S}^t(\Psi_x^s, :) = \widehat{S}^t(\Psi_x^s, :) + W_x\widehat{Z}_x$;
$W^t(\Psi_x^s, :) = W^t(\Psi_x^s, :) + W_x$;
end for
$I = \text{zeros}\left(M+\sqrt{P}-1, N+\sqrt{P}-1\right)$; $Q = I$;
/*The weighted averaging of the aggregate estimates of each pixel */
for each a,b = 1 to $\sqrt{P}$ **do**
$id = (b-1)\times\sqrt{P} + a$;
Π_a = a: M + a − 1; Π_b = b: N + b − 1;
$I(\Pi_a, \Pi_b) = I(\Pi_a, \Pi_b) + \text{reshape}\left(\widehat{S}^t(:, id), [M, N]\right)$;
$Q(\Pi_a, \Pi_b)$ = $Q(\Pi_a, \Pi_b)$ + reshape (W_t(:, id), [M, N]);
end for
$\widehat{S}^t = I/Q$;
$\widehat{S}^f = \text{WienerFiltering}\left(\widehat{S}^t\right)$; /*The empirical Wiener filtering */

The proposed algorithm can be summarized as follows. Let $\mathbf{Y}$ denote an observed noisy image with its coordinate domain $\mathbf{X} \in \mathbf{R}^{M\times N}$. First, for each pixel $y(x)$ and its target patch $\mathbf{Y}_x$, the corresponding patch group Z_x^v is formed by finding similar patches in a local search window. Next, after performing singular value decomposition (SVD) of the patch group $\bar{Z}_x^v$, the signal dimension K is determined by parallel analysis applied to the singular values λ for separating the signal and the noise in the SVD domain. Then, after the inverse SVD transform, the denoised patch group $\hat{Z}_x$ is obtained by the low-rank approximation, where most of the noise is eliminated. After that, the whole denoised image $\hat{S}^t$ is acquired by the weighted averaging of all the estimates of each pixel for further noise removal. Finally, after the shrinkage coefficients G_{Ω_x} are reconstructed from the power spectrum of 3D transform of the denoised image $\hat{S}^t$, the final noiseless image $\hat{S}^f$ is obtained by the collaborative Wiener filtering for further noise reduction.

3. Results and analysis

In this work, numerical simulation and experimental studies were carried out to verify the performance of the proposed algorithm subjectively and objectively. In the objective evaluation, the full-reference image quality assessment (FR-IQA) was adopted for synthetic images in numerical simulation, whereas the no-reference image quality assessment (NR-IQA) was used for real MR images in the experiments.

3.1. Simulation results on synthetic images

To test the performance of the proposed algorithm comprehensively, we have implemented the qualitative and quantitative evaluation on multiple test images from standard image databases [46]. The corrupted images synthetically damaged by white Gaussian noise using the noise model (1). For variant noise levels, the benchmark for image denoising evaluation includes the noise-free test images shown in Fig. 4.

A quantitative comparison was performed between the performances of the proposed denoising algorithm and the state-of-the-art methods published recently [9,10,54]. The well-known full-reference quality metrics were considered for measuring the similarity between the filtered image and the original noise-free image in terms of noise suppression and edge preservation, respectively. Both Peak Signal-to-Noise Ratio (PSNR) [25] and Structural SIMilarity (SSIM) [45] were adopted to evaluate noise suppression performance of different denoising methods, respectively. The edge preservation performance of different denoising methods was also quantified by the edge preservation index called Figure of Merit (FOM) [48,50], respectively. The FOM [48,50] is defined as

$$\mathrm{FOM} = \frac{1}{\max(n_d, n_r)} \sum_{i=1}^{n_d} \frac{1}{1+\gamma d_i^2} \tag{16}$$

where n_d is the number of detected edge pixels in the test noisy image, n_r is the number of reference edge pixels in the noise-free image, d_i is the Euclidean distance between the ith detected edge pixel and the nearest reference edge pixel, and $\gamma$is a constant typically set to 1/9. The Laplacian of Gaussian method was used to detect the edges.

In this simulation, the test images were degraded by Gaussian noise with zero means and different deviation 10,20,30 and 50, respectively. To verify the performances of noise suppression and edge preservation, our developed algorithm was compared with the current state-of-the-art methods, such as BM3D [9], PLPCA [10] and LPG-PCA [54]. The SSIM results for these test images are presented in Table 1. And the FOM results for these test images are also given in Table 2. To further inspect

Fig. 4. The test images in our experiments, from left to right, top to bottom: *Lena*, *Baboon*, *Barbara*, *Boat*, *Bridge*, *Monarch*, *House*, and *Brain*. These images present a wide range of edges, textures, details, and frequencies.

Table 1
The SSIM results of BM3D [9], PLPCA [10], LPG-PCA [54], and the proposed algorithm separately applied on subset of test images, e.g., *Lena*, *Baboon*, *Barbara*, *Boat*, *Bridge*, *Monarch*, *House*, and *Brain*. These noise-free images are corrupted by Gaussian noise with variant noise levels σ_n = 10, 20, 30, and 50, respectively. Top left: BM3D [9], Top right: PLPCA [10], Bottom left: LPG-PCA [54], Bottom right: Proposed. The best result among them is highlighted in each cell.

σ_n	10		20		30		50	
Lena	**.9169**	.9078	**.8767**	.8538	**.8440**	.7956	**.7987**	.6286
512 × 512	.9145	.9162	.8728	.8664	.8380	.8424	.7774	.7884
Baboon	.8900	**.8950**	.7801	.7714	.6830	.6676	.5320	.5199
512 × 512	.8844	.8770	.7642	**.7909**	.6562	**.7049**	.5116	**.5762**
Barbara	.9418	.9337	**.9046**	.8802	.8665	.8233	.7928	.6792
512 × 512	.9407	**.9421**	.8991	.8990	.8543	**.8717**	.7667	**.8014**
Boat	.8874	.8875	**.8265**	.8065	**.7789**	.7375	**.6996**	.5878
512 × 512	.8822	**.8920**	.8111	.8261	.7540	.7774	.6698	.6962
Bridge	**.9068**	.9059	.7904	.7789	.6963	.6818	.5695	.5447
512 × 512	.9004	.8926	.7742	**.7930**	.6701	**.7065**	.5390	**.5905**
Monarch	**.9560**	.9423	**.9210**	.8915	**.8865**	.8360	**.8239**	.6910
256 × 256	.9551	.9533	.9154	.9120	.8782	.8802	.7994	.8118
House	.9199	.9032	**.8726**	.8469	**.8489**	.7940	**.8154**	.6283
256 × 256	.9122	**.9201**	.8684	.8640	.8388	.8391	.7867	.7996
Brain	**.9010**	.8921	.8325	.7987	.7796	.7214	.6846	.5501
256 × 256	.8963	.8992	.8189	**.8329**	.7557	**.7797**	.6569	**.6954**
Average	**.9150**	.9084	**.8506**	.8285	.7980	.7571	.7146	.6037
	.9107	.9116	.8405	.8480	.7807	**.8002**	.6884	**.7199**

Table 2
The FOM results of BM3D [9], PLPCA [10], LPG-PCA [54], and the proposed algorithm separately applied on subset of test images, e.g., *Lena*, *Baboon*, *Barbara*, *Boat*, *Bridge*, *Monarch*, *House*, and *Brain*. These noise-free images are corrupted by Gaussian noise with variant noise levels σ_n = 10, 20, 30, and 50, respectively. Top left: BM3D [9], Top right: PLPCA [10], Bottom left: LPG-PCA [54], Bottom right: Proposed. The best result among them is highlighted in each cell.

σ_n	10		20		30		50	
Lena	.9168	**.9210**	.8463	.8207	.7965	.7713	.6776	.6984
512 × 512	.8913	.9195	.7932	**.8619**	.7353	**.8133**	.6283	**.7128**
Baboon	**.9470**	.9416	.8712	.8464	.7861	.7524	.6231	.6890
512 × 512	.9312	.9368	.8458	**.8767**	.7725	**.8071**	.6644	**.6949**
Barbara	**.9480**	.9394	.8686	.8304	.8162	.7649	.6878	.6907
512 × 512	.9241	.9406	.8042	**.8758**	.7329	**.8291**	.6336	**.7407**
Boat	**.9318**	.9254	.8354	.7970	.7672	.7168	.6245	.6521
512 × 512	.8919	.9313	.7573	**.8499**	.6650	**.7854**	.5514	**.6718**
Bridge	**.9426**	.9397	.8504	.8186	.7427	.7067	.5724	**.6121**
256 × 256	.9210	.9300	.8007	**.8510**	.6865	**.7607**	.5400	.5724
Monarch	.9728	**.9739**	.9135	.8936	**.8945**	.8709	.8093	.7978
256 × 256	.9658	.9711	.8795	**.9220**	.8410	.8937	.7587	**.8245**
House	.9394	**.9522**	.8994	.9001	.9078	.8912	.8180	.8321
256 × 256	.9263	.9403	.8679	**.9093**	.8209	**.9347**	.7284	**.8434**
Brain	**.9297**	.9159	.8046	.7529	.7588	.6875	.5698	.5676
256 × 256	.8858	.9286	.7219	**.8206**	.6486	**.7661**	.5045	**.5960**
Average	**.9410**	.9386	.8612	.8325	.8087	.7702	.6728	.6925
	.9172	.9373	.8088	**.8709**	.7378	**.8238**	.6262	**.7071**

the effectiveness of our proposed algorithm, the detailed denoised results of the proposed algorithm, BM3D [9], PLPCA [10], and LPG-PCA [54] for the fragments of the *Lena*, *Baboon* and *Barbara* images are shown in Fig. 5–7, respectively.

As is shown in Table 1, the SSIM results of our proposed algorithm outperform those of PLPCA [10], and LPG-PCA [54] in most cases, and can be competitive with those of BM3D [9]. However, the FOM results in Table 2 shows that our proposed algorithm are generally superior to all of them in the edge preservation. The visual comparisons in Fig. 5–7 demonstrate that the proposed algorithm have better recovery of textures and edges than the baseline methods. Therefore, our proposed algorithm outperforms the best existing state-of-the-art methods, e.g., BM3D [9] not only in visual comparisons but also in the edge preservation in most cases. As can be seen from the simulation results, it works well for a wide variety of noisy images and can effectively produce sharp edges and rich textures.

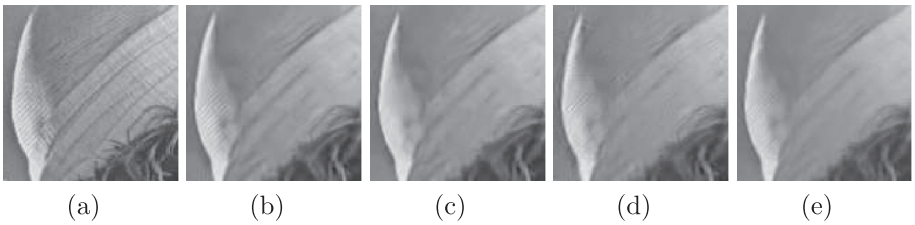

Fig. 5. Visual comparisons of the denoising results of the proposed algorithm and other state-of-the-art methods for the *Lena* image corrupted with Gaussian noise with standard deviation 30. From left to right: (a) original subimage; (b) the proposed algorithm (PSNR = 31.33 dB, SSIM = .8424); (c) BM3D [9] (PSNR = 31.20 dB, SSIM = .8440); (d) PLPCA [10] (PSNR = 30.26 dB, SSIM = .7956); and (e) LPG-PCA [54] (PSNR = 30.66 dB, SSIM = .8380).

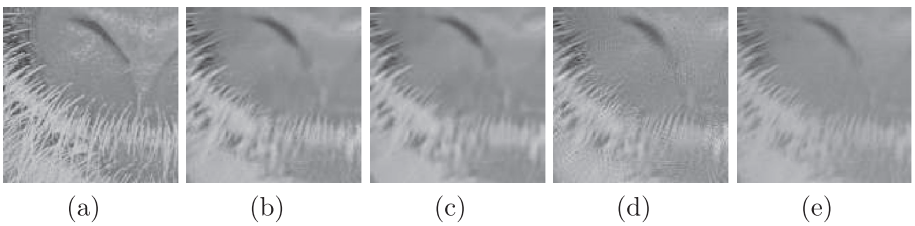

Fig. 6. Visual comparisons of the denoising results of the proposed algorithm and other state-of-the-art methods for the *Baboon* image corrupted with Gaussian noise with standard deviation 50. From left to right: (a) original subimage; (b) the proposed algorithm (PSNR = 23.46 dB, SSIM = .5762); (c) BM3D [9] (PSNR = 23.13 dB, SSIM = .5320); (d) PLPCA [10] (PSNR = 23.01 dB, SSIM = .5199); and (e) LPG-PCA [54] (PSNR = 22.83 dB, SSIM = .5116).

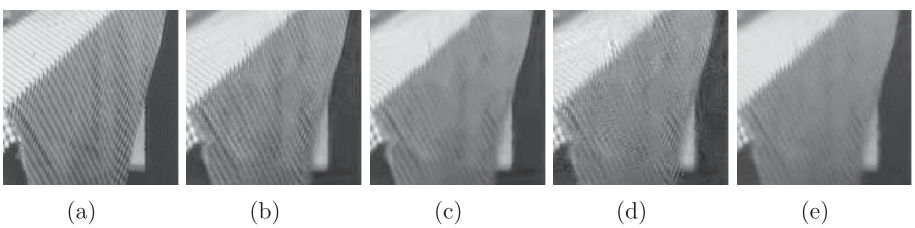

Fig. 7. Visual comparisons of the denoising results of the proposed algorithm and other state-of-the-art methods for the *Barbara* image corrupted with Gaussian noise with standard deviation 50. From left to right: (a) original subimage; (b) the proposed algorithm (PSNR = 27.54 dB, SSIM = .8014); (c) BM3D [9] (PSNR = 27.21 dB, SSIM = .7928); (d) PLPCA [10] (PSNR = 25.98 dB, SSIM = .6792); and (e) LPG-PCA [54] (PSNR = 26.20 dB, SSIM = .7667).

3.2. Experimental results on real MR images

Besides the simulations on noisy synthetic images, we also validated our denoising algorithm on real MR images because the characteristics of the fine structures (especially the edges and the textures) in MR images is very important for medical diagnosis. In this experiment, the real MR images were acquired from the MR scanner at 3T (MAGNETOM Tim Trio, Siemens, Germany). As objective no-reference image quality metric, the signal-to-noise ratio (SNR) [11,19,49] was used for measuring the noise in an input noisy MR image and the denoised results of the proposed algorithm and the current popular methods [9,10,54], respectively. The measurement of SNR in MR images is commonly based on the signal statistics in two separate regions of interest (ROIs) from a single image: one in the tissue of interest, and one in background air. The SNR [11,19,49] was defined as

$$\mathrm{SNR}_{\mathrm{stdv}} = \frac{S_{\mathrm{mean}}}{\sigma_{\mathrm{stdv}}} \tag{17}$$

Table 3
The four pulse sequences used in the human experiments with these imaging parameters, i.e., Repetition Time (TR) (ms), Echo Time (TE) (ms), Flip Angle (FA) (°), Echo Train Length (ETL), Slice Thickness (ST) (mm), and Pixel Bandwidth (PB) (Hz).

Images	Sequence	TR	TE	FA	ETL	ST	PB
T1_SE	SE	2000	131	120	37	0.36	449
TOF	SE	327	14	90	1	3	130
TSE_T1	GR	19	3.09	25	1	0.70	250
TSE_T2	SE	1120	26	174	7	2	130

Table 4
The SNR results of the comparison between the proposed algorithm and BM3D [9], PLPCA [10], and LPG-PCA [54] for the four noisy MR images, i.e., *T1_SE*, *TOF*, *TSE_T1*, and *TSE_T2*.

Images	Noisy	Proposed	BM3D[9]	PLPCA[10]	LPG-PCA[54]
T1_SE	24.77	190.85	183.40	124.37	458.53
TOF	27.40	77.90	71.98	39.59	116.30
TSE_T1	12.21	116.47	102.72	102.21	168.96
TSE_T2	15.51	293.25	221.83	83.86	502.28

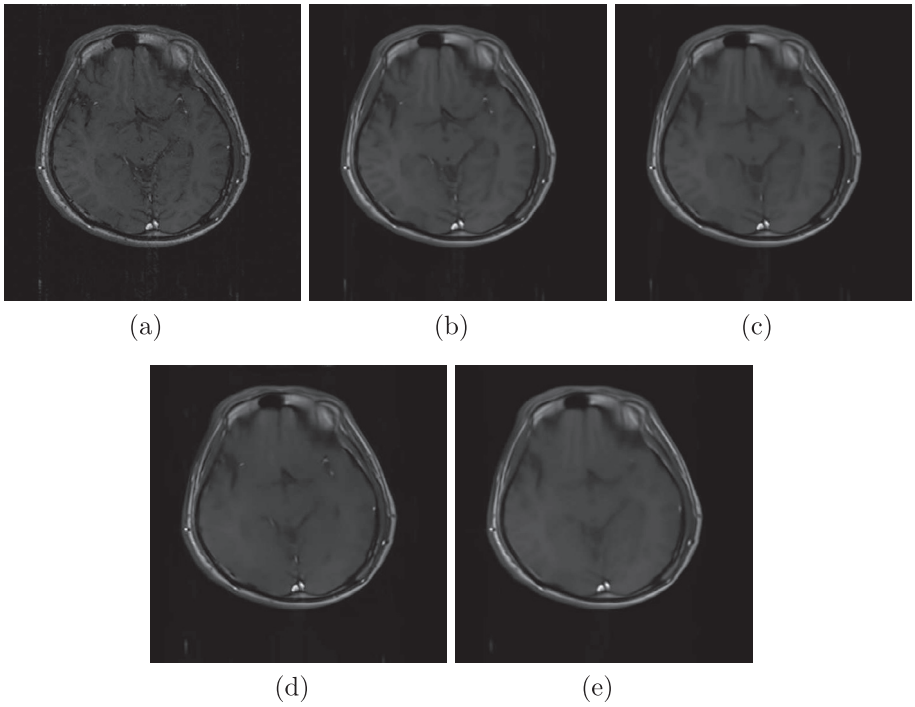

Fig. 8. Visual comparisons of the denoising results of the proposed algorithm and other state-of-the-art methods for the *T1_SE* MR images. From left to right: (a) noisy MR images; (b) the proposed algorithm; (c) BM3D [9]; (d) PLPCA [10]; and (e) LPG-PCA [54].

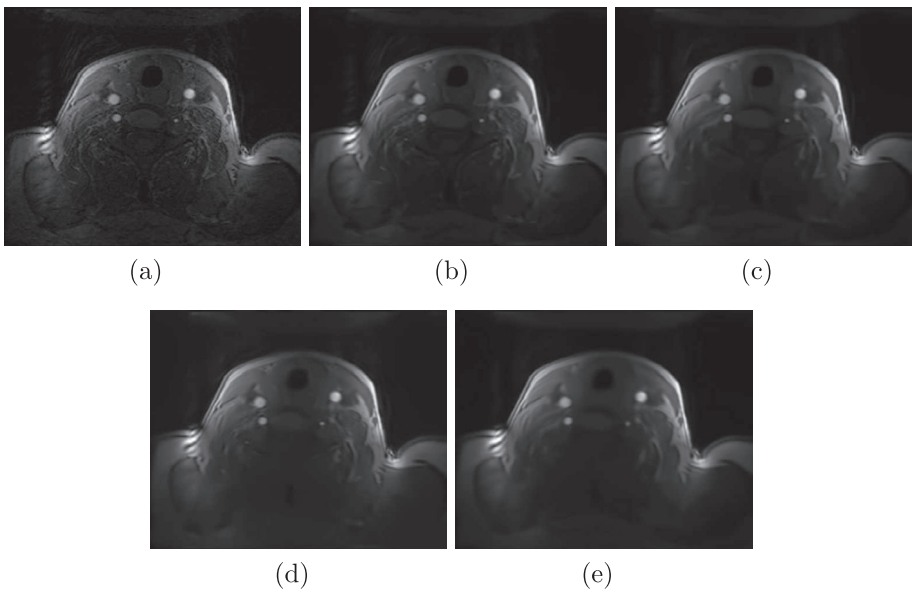

Fig. 9. Visual comparisons of the denoising results of the proposed algorithm and other state-of-the-art methods for the *TOF* MR images. From left to right: (a) noisy MR images; (b) the proposed algorithm; (c) BM3D [9]; (d) PLPCA [10]; and (e) LPG-PCA [54].

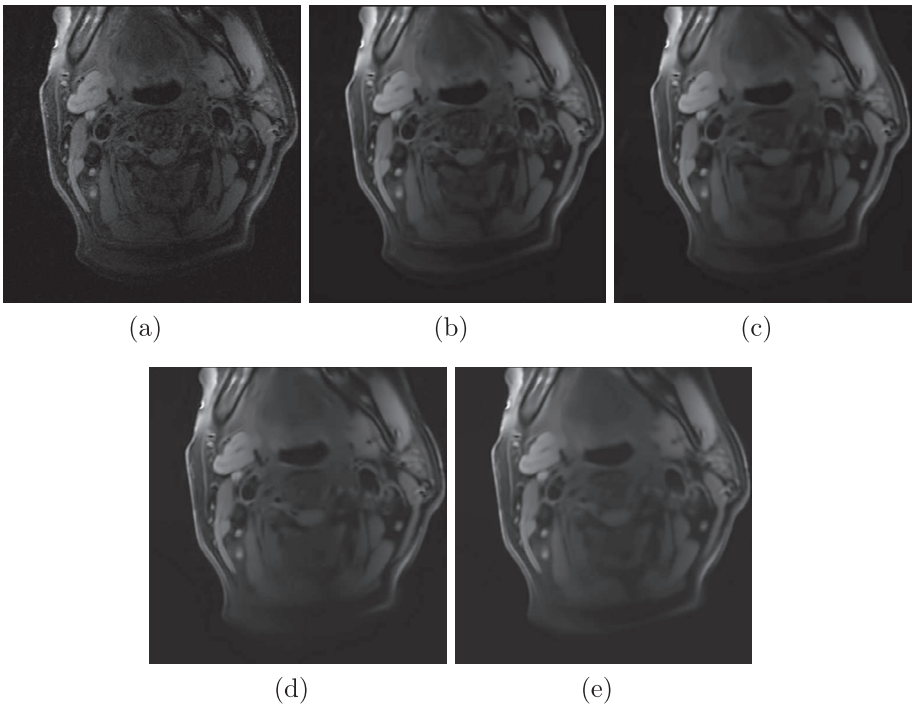

Fig. 10. Visual comparisons of the denoising results of the proposed algorithm and other state-of-the-art methods for the *TSE_T1* MR images. From left to right: (a) noisy MR images; (b) the proposed algorithm; (c) BM3D [9]; (d) PLPCA [10]; and (e) LPG-PCA [54].

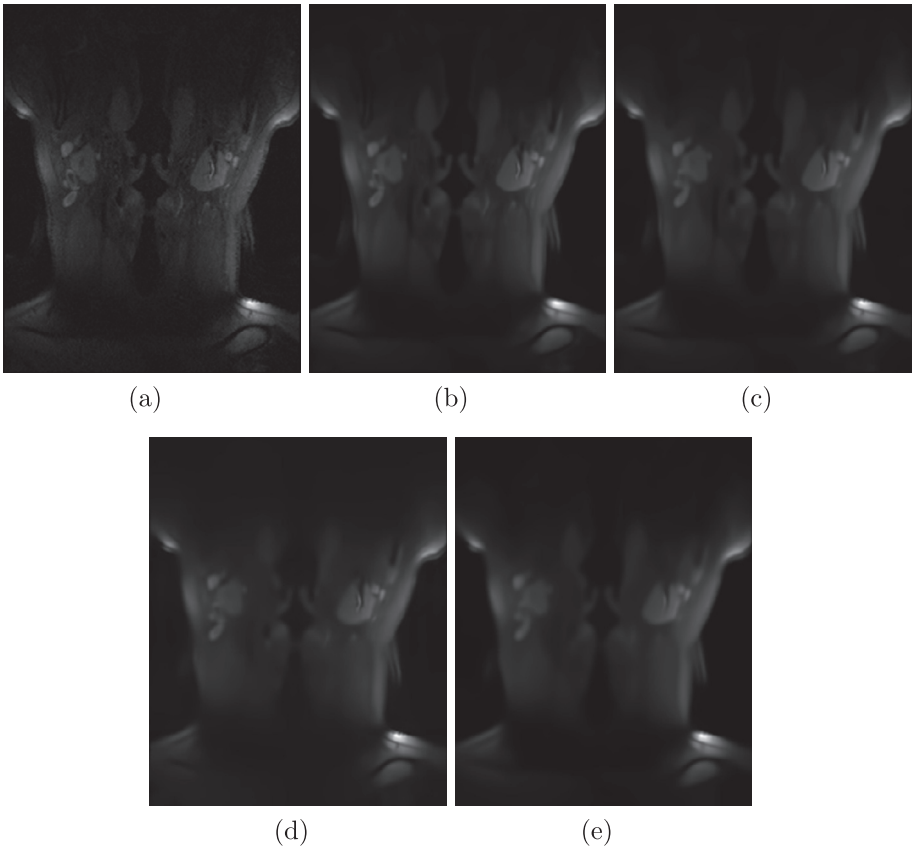

Fig. 11. Visual comparisons of the denoising results of the proposed algorithm and other state-of-the-art methods for the *TSE_T2* MR images. From left to right: (a) noisy MR images; (b) the proposed algorithm; (c) BM3D [9]; (d) PLPCA [10]; and (e) LPG-PCA [54].

where S_{mean} is the mean value of pixel intensities in a region of interest (ROI) within the object, and σ_{stdv} is the standard deviation of noise in a chosen background ROI outside the object, free from signals or ghosting artifacts.

The four volunteers with informed consent in accordance with our institution's human subject policies participated in the study. They were scanned with the four pulse sequences, i.e., spin echo (SE), turbo spin echo (TSE), and gradient echo (GR), whose imaging parameter values are given in Table 3. These four images, i.e., *T1_SE*, *TOF*, *TSE_T1*, and *TSE_T2*, provide a testing set which presents a good diversity: different anatomical structures, and different noise intensities. To show the robustness of the proposed algorithm with real MR images, we used the same parameters in all examples. Table 4 shows the SNR results of the comparison between the proposed algorithm and other state-of-the-art methods for the noisy MR images. Fig. 8–11 present the visual comparison results of the proposed algorithm, BM3D [9], PLPCA [10], and LPG-PCA [54] for the different noisy MR images, respectively.

As can be seen from Table 4, the SNR results of the proposed algorithm outperforms those of BM3D [9], and PLPCA [10], and are lower than those of LPG-PCA[54]. However, the visual comparisons of these denoising methods in Fig. 8–11 show that LPG-PCA[54] smooths out the edges and anatomical structures of MR images. It is observed that the results of our proposed algorithm have sharper edges and clearer anatomical structures than those of the state-of-the-art methods. Strictly speaking, in fact the AWGN model (1) is not very accurate to describe the noise in MR images. The Gaussian assumption in the simulation on synthetic images maybe causes that the proposed algorithm does not outperform the existing best state-of-the-art methods in some cases, e.g., BM3D [9]. These experiments verify that the proposed algorithm can be effectively applied to noisy MR images with different noise levels for noise removal, and achieves a better edge and structure preservation than other state-of-the-art methods.

4. Conclusions and future work

In this paper, we addressed the problem of automatically determining the signal dimensionality for the similar patch groups from the given noisy image. For a pixel in the search window, the parallel analysis with Monte Carlo simulation is employed to estimate the signal component dimensionality from its related high-dimensional noisy patch groups. After the inverse SVD transform, the approximation of the true noiseless patch groups is obtained by the low-rank approach. Thus, our proposed adaptive PCA can discard a considerable part of noises almost without loss of signal information. The weighted averaging aggregation operator is used to reduce noise further. Then, the reconstructed noise-free image with better denoising performance is achieved by the empirical Wiener filtering applied to the first-stage denoised image. The experimental results of real MR images demonstrate that the proposed denoising algorithm can outperform the best state-of-the-art methods both visually and quantitatively, especially for image regions containing the abundant edges, and the fine structures. Moreover, our proposed adaptive PCA approach can be extended to many applications, particularly multivariate analysis and machine learning. Finally, combined with sparse representation, the proposed algorithm will be further studied on the optimal parameters of the search window, the patch size and its shape in the future.

Acknowledgements

This work was supported by National Natural Science Foundation of China under Contract No. 61201442, China Postdoctoral Science Foundation funded project under Contract No. 2013M530481 and Doctoral Fund of Ministry of Education of China under Contract No. 20110001120117.

References

[1] M. Aharon, M. Elad, A.M. Bruckstein, K-SVD: an algorithm for designing of overcomplete dictionaries for sparse representation, IEEE Transactions on Signal Processing 54 (11) (2006) 4311–4322.
[2] D. Alassi, R. Alhajj, Effectiveness of template detection on noise reduction and websites summarization, Information Sciences 219 (2013) 41–72.
[3] R.C. Amorim, B. Mirkin, Minkowski metric, feature weighting and anomalous cluster initializing in K-Means clustering, Pattern Recognition 45 (3) (2012) 1061–1075.
[4] R. Bernardes, C. Maduro, P. Serranho, A. Araujo, S. Barbeiro, J. Cunha-Vaz, Improved adaptive complex diffusion despeckling filter, Optics Express 18 (23) (2010) 24048–24059.
[5] A. Buades, B. Coll, J.M. Morel, A review of image denoising algorithms with a new one, Multiscale Modeling and Simulation 4 (2) (2005) 490–530.
[6] S.G. Chang, B. Yu, M. Vetterli, Adaptive wavelet thresholding for image denoising and compression, IEEE Transactions on Image Processing 9 (9) (2000) 1532–1546.
[7] P. Chatterjee, P. Milanfar, Is denoising dead?, IEEE Transactions on Image Processing 19 (4) (2010) 895–911
[8] A.D. Cheveigne, J.Z. Simon, Denoising based on spatial filtering, Journal of Neuroscience Methods 171 (2) (2008) 331–339.
[9] K. Dabov, A. Foi, V. Katkovnik, K. Egiazarian, Image denoising by sparse 3D transform-domain collaborative filtering, IEEE Transactions on Image Processing 16 (8) (2007) 2080–2095.
[10] C.A. Deledalle, J. Salmon, A.S. Dalalyan, Image denoising with patch based PCA: local versus global, in: Proceedings of the British Machine Vision Conference 2011 (BMVC), vol. 63 (3), 2011, pp. 782–789.
[11] O. Dietrich, J.G. Raya, S.B. Reeder, M.F. Reiser, S.O. Schoenberg, Measurement of signal-to-noise ratios in MR images: influence of multichannel coils, parallel imaging, and reconstruction filters, Journal of Magnetic Resonance Imaging 26 (2) (2007) 375–385.
[12] Y. Ding, Y.C. Chung, O.P. Simonetti, A method to assess spatially variant noise in dynamic MR image series, Magnetic Resonance in Medicine 63 (3) (2010) 782–789.
[13] D.L. Donoho, De-noising by soft-thresholding, IEEE Transactions on Information Theory 41 (3) (1995) 613–627.
[14] M. Elad, M. Aharon, Image denoising via sparse and redundant representations over learned dictionaries, IEEE Transactions on Image Processing 15 (12) (2006) 3736–3745.

[15] A. Foi, V. Katkovnik, K. Egiazarian, Pointwise shape-adaptive DCT for high-quality denoising and deblocking of grayscale and color images, IEEE Transactions on Image Processing 16 (5) (2007) 1395–1411.
[16] B.J. Frey, D. Dueck, Clustering by passing messages between data points, Science 315 (2007) 972–976.
[17] S. Gezici, I. Yilmaz, O.N. Gerek, A.E. Cetin, Image denoising using adaptive subband decomposition, in: Proceedings of International Conference on Image Processing (ICIP), Thessaloniki 1, October 7–10, 2001, pp. 261–264.
[18] M. Ghazal, A. Amer, A. Ghrayeb, Structure-oriented multidirectional wiener filter for denoising of image and video signals, IEEE Transactions on Circuits and Systems for Video Technology 18 (12) (2008) 1797–1802.
[19] G. Gilbert, Measurement of signal-to-noise ratios in sum-of-squares MR images, Journal of Magnetic Resonance Imaging 26 (6) (2007) 1678.
[20] H. Gudbjartsson, S. Patz, The Rician distribution of noisy MRI data, Magnetic Resonance in Medicine 34 (6) (1995) 910–914.
[21] XiaoHong Han, XiaoMing Chang, An intelligent noise reduction method for chaotic signals based on genetic algorithms and lifting wavelet transforms, Information Sciences 218 (1) (2013) 103–118.
[22] Y.M. He, T. Gan, W.F. Chen, H.J. Wang, Adaptive denoising by singular value decomposition, IEEE Signal Processing Letters 18 (4) (2011) 215–218.
[23] K. Hirakawa, T.W. Parks, Image denoising using total least squares, IEEE Transactions on Image Processing 15 (9) (2006) 2730–2742.
[24] J.L. Horn, A rationale and test for the number of factors in factor analysis, Psychomerica 30 (2) (1965) 179–185.
[25] Q. Huynh-Thu, M. Ghanbari, Scope of validity of PSNR in image/video quality assessment, Electronics Letters 44 (13) (2008) 800–801.
[26] K.W. Jorgensen, L.K. Hansen, Model selection for Gaussian kernel PCA denoising, IEEE Transactions on Neural Networks and Learning Systems 23 (1) (2012) 163–168.
[27] K. Kose, V. Cevher, A.E. Cetin, Filtered variation method for denoising and sparse signal processing, in: Proceedings of IEEE International Conference on Acoustics, Speech and Signal Processing (ICASSP), Kyoto, 25–30, 2012, pp. 3329–3332.
[28] Chul Lee, Chulwoo Lee, Chang-Su Kim, An MMSE approach to nonlocal image denoising: theory and practical implementation, Journal of Visual Communication and Image Representation 23 (3) (2012) 476–490.
[29] A. Lev, S.W. Zucker, A. Rosenfeld, Iterative enhancemnent of noisy images, IEEE Transactions on Systems, Man and Cybernetics 7 (6) (1977) 435–442.
[30] T.C. Lin, A new adaptive center weighted median filter for suppressing impulsive noise in images, Information Sciences 177 (4) (2007) 1073–1087.
[31] Matteo Maggioni, Vladimir Katkovnik, Karen Egiazarian, Alessandro Foi, A nonlocal transform-domain filter for volumetric data denoising and reconstruction, IEEE Transactions on Image Processing 22 (1) (2013) 119–133.
[32] J.V. Manjon, P. Coupe, L. Marti-Bonmati, D.L. Collins, M. Robles, Adaptive non-local means denoising of MR images with spatially varying noise levels, Journal of Magnetic Resonance Imaging 31 (1) (2010) 192–203.
[33] I. Markovsky, Low-rank Approximation: Algorithms, Implementation, Applications, Springer, 2012.
[34] N.E. Nahi, Role of recursive estimation in statistical image enhancement, Proceedings of the IEEE 60 (7) (1972) 872–877.
[35] J. Portilla, V. Strela, M.J. Wainwright, E.P. Simoncelli, Image denoising using scale mixtures of Gaussians in the wavelet domain, IEEE Transactions on Image Processing 12 (11) (2003) 1338–1351.
[36] T. Qiu, A. Wang, N. Yu, A. Song, LLSURE: local linear SURE-based edge-preserving image filtering, IEEE Transactions on Image Processing 22 (1) (2013) 80–90.
[37] L.I. Rudin, S.J. Osher, E. Fatemi, Nonlinear total variation based noise removal algorithms, Physica D 60 (1–4) (1992) 259–268.
[38] J. Rydell, H. Knutsson, M. Borga, Bilateral filtering of fMRI data, IEEE Journal of Selected Topics in Signal Processing 2 (6) (2008) 891–896.
[39] E.P. Simoncelli, E.H. Adelson, Noise removal via Bayesian wavelet coring, Proceedings of 3rd IEEE International Conference on Image Processing (1996) 379–382.
[40] J.L. Starck, E.J. Candes, D.L. Donoho, The curvelet transform for image denoising, IEEE Transactions on Image Processing 11 (6) (2002) 670–684.
[41] H. Takeda, S. Farsiu, P. Milanfar, Kernel regression for image processing and reconstruction, IEEE Transactions on Image Processing 16 (2) (2007) 349–366.
[42] T. Tasdizen, Principal neighborhood dictionaries for non-local means image denoising, IEEE Transactions on Image Processing 18 (12) (2009). 2649-2260.
[43] D. Van De Ville, M. Kocher, SURE-based non-local means, IEEE Signal Processing Letters 16 (11) (2009) 973–976.
[44] L.J.P. van der Maaten, E.O. Postma, H.J. van den Herik, Dimensionality Reduction: A Comparative Review, Tilburg University Technical Report, TiCC-TR 2009-005, 2009.
[45] Z. Wang, A.C. Bovik, H.R. Sheikh, E.P. Simoncelli, Image quality assessment: from error visibility to structural similarity, IEEE Transactions on Image Processing 13 (4) (2004) 600–612.
[46] Image database maintained by Computer Vision Group. University of Granada, March 22, 2013. <http://decsai.ugr.es/cvg/dbimagenes/>.
[47] Siep Weiland, Femke van Belzen, Singular value decompositions and low rank approximations of tensors, IEEE Transactions on Signal Processing 58 (3) (2010) 1171–1182.
[48] Y. Yu, S.T. Acton, Speckle reducing anisotropic diffusion, IEEE Transactions on Image Processing 11 (11) (2002) 1260–1270.
[49] J. Yu, H. Agarwal, M. Stuber, M. Schar, Practical signal-to-noise ratio quantification for sensitivity encoding: application to coronary MRA, Journal of Magnetic Resonance Imaging 33 (6) (2011) 1330–1340.
[50] Y. Yue, M.M. Croitoru, A. Bidani, J.B. Zwischenberger, J.W. Clark, Nonlinear multiscale wavelet diffusion for speckle suppression and edge enhancement in ultrasound images, IEEE Transactions Medical Imaging 25 (3) (2006) 297–311.
[51] Lihi Zelnik-Manor, Kevin Rosenblum, Yonina C. Eldar, Dictionary optimization for block-sparse representations, IEEE Transactions on Signal Processing 60 (5) (2012) 2386–2395.
[52] Li Zhang, S. Vaddadi, Hailin Jin, S.K. Nayar, Multiple view image denoising, in: IEEE Conference on Computer Vision and Pattern Recognition (CVPR) 20–25, 2009, pp. 1542–1549.
[53] Y.Q. Zhang, Y. Ai, K.J. Dai, G.D. Zhang, Grey model via polynomial for image denoising, Journal of Grey System 22 (2) (2010) 117–128.
[54] L. Zhang, W. Dong, D. Zhang, G. Shi, Two-stage image denoising by principal component analysis with local pixel grouping, Pattern Recognition 43 (4) (2010) 1531–1549.
[55] Yong-Qin Zhang, Yu Ding, Jiaying Liu, Zongming Guo, Guided image filtering using signal subspace projection, IET Image Processing 7 (3) (2013) 270–279.
[56] Yong-Qin Zhang, Yu Ding, Jin-Sheng Xiao, Jiaying Liu, Zongming Guo, Visibility enhancement using an image filtering approach, EURASIP Journal on Advances in Signal Processing 2012:220 (2012) 1–6.